Photo-induced synthesis of polymeric nanoparticles and chemiluminescent degradable materials *via* flow chemistry†

Joshua O. Holloway, ‡[ab] Laura Delafresnaye, ‡*[ab] Emily M. Cameron, [ab] Jochen A. Kammerer [ab] and Christopher Barner-Kowollik *[abc]

We report the photo-induced, additive-free, continuous synthesis of polymeric particles using flow chemistry. Not only can these particles be formed under ambient conditions in a solely light-induced precipitation polymerisation, they can be prepared *via* continuous flow techniques to up-scale the synthetic process. We carefully assess the flow chemical parameters and analyse the resulting particles quantitatively using scanning electron microscopy (SEM). Particle formation is a direct result of the step-growth polymerisation *via* a photochemically induced AA + BB Diels–Alder reaction, which we herein base on the dialdehyde monomer (AA) derived from the sustainable precursor, thymol. By employing a peroxyoxalate bismaleimide (BB), we introduce particles that can be selectively degraded on-demand, self-reported by light emission through chemiluminescence.

New concepts

We present the additive-, radical-, and surfactant-free synthesis of non-crosslinked polymeric particles *via* precipitation polymerisation in dispersed media utilising continuous photoflow synthesis. The successful transposition of photo-induced step-growth polymerisation from batch to a continuous process allows for the production of particles on a larger scale, expanding the potential for industrial applications. Our method, therefore, represents a radical new approach towards the synthesis of polymeric particles. The incorporation of a chemiluminescent bifunctional molecule further enables the synthesis of nanoparticles that, upon the addition of H_2O_2, undergo degradation accompanied by light emission through chemiluminescence. Polymer-supported chemiluminescence remains relatively unexplored and the synthesis of such nanoparticles could pave the way towards applications in bioimaging, therapeutics or point-of-care devices, particularly with respect to the monitoring of H_2O_2.

Introduction

The demand for polymeric nano- and microparticles has steadily increased over the past decades, which is in part because of their versatility in terms of size, morphology, and functionality. Their properties make them particularly attractive for applications ranging from chromatographic separation, point-of-care testing devices, coatings or drug delivery systems.[1–4] Typically, polymeric nano- and microparticles are prepared *via* heterogenous polymerisation techniques such as (mini)emulsion, suspension or dispersion.[5,6] However, these techniques require a stabiliser or surfactant to ensure the colloidal stability of the particles. Precipitation polymerisation has gained more traction recently, as this technique does not require any of the aforementioned additives, therefore providing surface-clean particles, along with the advantage of additive-free synthesis.[7,8] First described in the 1980s[9,10] and then extensively studied by Stöver and co-workers,[11] the mechanism relies on the aggregation of soluble oligomers in a θ-solvent (*i.e.* the solvent dissolves the monomers, but behaves as a non-solvent for the polymer) during the nucleation period, which subsequently desolvates to form particle nuclei. The particles subsequently grow by continuously capturing soluble (or highly swollen) oligomeric species, which concomitantly stabilise the particles.[11] Several methodologies employing either thermal or photoactive initiators have been developed to form porous, hollow, core–shell or highly functional particles.[12] Other examples of particle synthesis by precipitation polymerisation are the formation of particles following polycondensation reactions.[13,14] Photoinduced precipitation polymerisation is of

[a] *School of Chemistry and Physics, Queensland University of Technology (QUT), 2 George Street, Brisbane, QLD 4000, Australia. E-mail: laura.delafresnaye@qut.edu.au, christopher.barnerkowollik@qut.edu.au*
[b] *Centre for Materials Science, Queensland University of Technology (QUT), 2 George Street, Brisbane, QLD 4000, Australia*
[c] *Institute of Nanotechnology (INT), Karlsruhe Institute of Technology (KIT), Hermann-von-Helmholtz-Platz 1, 76344 Eggenstein-Leopoldshafen, Germany*

‡ These authors contributed equally.

particular interest since the reaction is carried out at room temperature with all the advantages of photochemistry such as spatiotemporal control. Photoinitiators of type I[15 17] or II[18,19] are generally employed, therefore producing particles *via* free or controlled radical chain growth polymerisation.

Our group has developed a technology platform to form particles *via* a light induced step-growth polymerisation without any initiators or radical formation. Previously, we synthesised photo-crosslinkable soluble pre-polymers (*e.g.* poly(styrene)[20 22] and poly(methyl methacrylate)[23]), which can react with a suitable bifunctional linker to form monodisperse particles under light irradiation (λ = 320 to 525 nm). Most recently, we have reported the synthesis of particles by simply activating a photoactive AA-type monomer (see Fig. 1) under a 365 nm LED[24] or sunlight,[25] which subsequently reacted with a suitable bifunctional BB-type monomer *via* a Diels–Alder (DA) step-growth polymerisation. Upon irradiation, the photoactive AA monomer successively forms two highly reactive *ortho*-quinodimethane (*o*-QDM) moieties, which subsequently react with the BB monomer *via* a Diels–Alder [4+2] cycloaddition. The resulting step-growth polymerisation forms $[AABB]_x$ oligomers, which eventually reach a critical molecular weight and phase-separate from the continuous medium to form nuclei. These nuclei grow by capturing more and more oligomers, forming stable polymeric particles (the formation of which can be confirmed by scanning electron microscopy – SEM). However, despite the novelty and key advances demonstrated in our previously reported study, it remained limited in scope due to the small scale and comparatively long reaction times of batch synthesis along with the sensitive nature of precipitation polymerisation, in particular related to the need to employ a low stirring rate to avoid aggregation and encourage uniform particle formation.[19]

One key challenge in precipitation polymerisation is scalability and efficiency as the monomer loading is typically low and the reaction times can vary from a few hours to a few days. Continuous flow reactors represent a viable option as they offer faster reaction times, increased yields and the ability to control more reaction parameters compared to conventional batch methods.[26,27] Photoflow polymerisation combines the benefits of flow chemistry and photopolymerisation, allowing for the rapid and efficient synthesis of a wide range of polymeric materials.[28] Critically, the largest hurdle of batch photopolymerisation in dispersed media is the optical opacity of the solution, caused by light scattering from the formed particles, ultimately limiting the light penetration depth.[29,30] The scattering effect can be reduced by decreasing the optical path length – whilst enabling even light irradiation throughout the sample – and increasing the surface area to volume ratio of the reaction vessel. It should be noted however, that whilst reducing the optical path length appears to be straightforward, the resulting increase of the surface area may lead to reactor fouling, which is one of the most significant challenges in continuous heterogeneous processes. Recently, some studies have successfully translated photopolymerisation in heterogenous media to flow reactors.[31] For example,

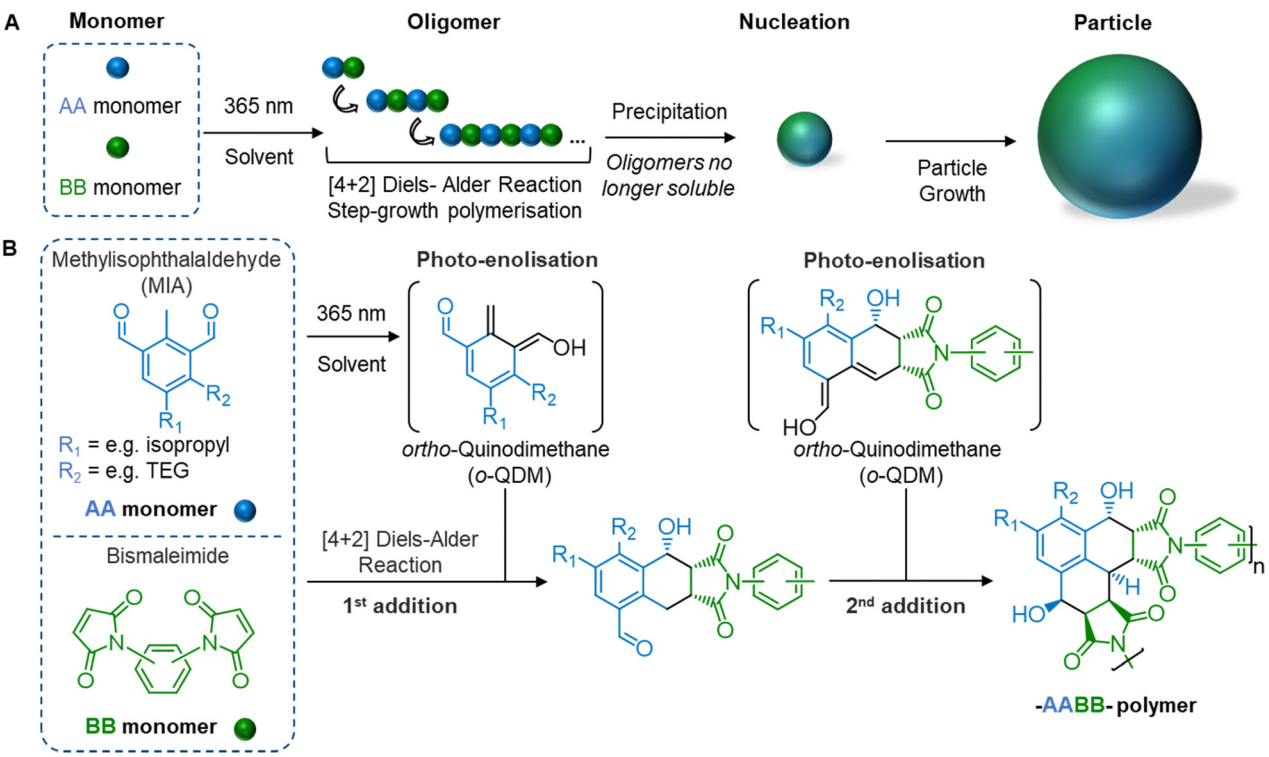

Fig. 1 (A) Overview of the particle formation. Under irradiation, AA and BB monomers react *via* a photoinduced [4+2] Diels–Alder cycloaddition to form step-growth oligomers. Once the oligomers have reached a critical molecular weight in which they are no longer soluble in the θ-solvent, they precipitate from solution to form nuclei which subsequently grow by capturing oligomers. (B) Chemical structure of the AA and BB monomers and the corresponding polymers.

sphere, worm, and vesicle morphologies were obtained *via* visible light-initiated polymerisation-induced self-assembly (PISA) using continuous flow reactors with higher control in comparison to conventional batch procedures.[32] However, this realm is relatively underexplored.[28]

In the present work, we employ a photoflow reactor to produce polymeric particles in large quantity from a homogenous reaction mixture. We achieve this *via* a photochemically induced step-growth DA precipitation polymerisation, using an AA-type and a BB-type monomer (Fig. 1). We investigate several parameters such as the solvent combination, flow rate, and concentration to ultimately produce over 0.5 g of material in one reaction. To demonstrate the further potential of our approach, we exploit the nanoparticles as self-reporting, chemiluminescent (CL) materials. Chemiluminescence is the emission of light as a result of a chemical reaction and a powerful tool for bioimaging, therapeutics or point-of-care devices.[33] While CL has been widely developed in analytical chemistry, polymer-supported CL has been barely exploited.[34] Our team has been particularly interested in the peroxyoxalate chemiluminescent (PO-CL) mechanism in which an aromatic oxalic ester reacts with hydrogen peroxide (H_2O_2) to form a high-energy intermediate *in situ* that spontaneously decomposes into carbon dioxide, subsequently releasing energy. Interestingly, this intermediate can transfer its electronic excitation energy to a nearby fluorophore, elevating the fluorophore to an excited state, thus releasing photons and emitting light when returning to its ground state. Intracellular H_2O_2 can regulate physiological events and monitoring its level is essential as an overexpression of H_2O_2 is often associated with cancerous cells, inflammation or other diseases.[33]

Importantly, the PO-CL reaction requires that the oxalate ester and the fluorophore are in close proximity to one another. We have thus designed a molecule bearing an oxalate ester and two maleimides as functional handles.[35] We have previously utilised the maleimides as dienophiles with a tetrazole compound to form a highly fluorescent pyrazoline adduct *via* a nitrile imine-mediated tetrazole–ene cycloaddition (NITEC) reaction.[36] The addition of H_2O_2, which resulted in a light emission of blue or yellow depending on the fluorophore used was further applied to the surface of poly(divinylbenzene) microparticles.[35] More recently, we formed CL degradable polystyrene microspheres by employing this peroxyoxalate–maleimide as a bifunctional linker to crosslink a poly(styrene-*co*-tetrazole) prepolymer.[37]

Herein, we report the upscaled, photochemical synthesis of polymeric particles using flow chemistry, and demonstrate how the introduction of a fluorescent Diels–Alder adduct can result in nanoparticles with chemiluminescent self-reporting properties.

Results and discussion

Monomer synthesis

Underpinned by our previous studies on the Diels–Alder cycloaddition of methylisophthalaldehydes,[24,25,38,39] we introduce a significant improvement in terms of the design of a sustainable photoactive AA-type monomer, eliminating acute toxic reagents and using a natural starting reagent: thymol, a monoterpenoid phenol derived from the natural resource *Thymus vulgaris* L., more commonly known as the herb, thyme. We used thymol (2-isopropyl-5-methylphenol) in lieu of 2,5-dimethylphenol as it differs only by an isopropyl group instead of a methyl group at the 2-position (Fig. 1B, R_1). Since this moiety is *para* relative to the photoreactive *ortho*-quinodimethane (*o*-QDM), no effect on the photochemical reactivity of the final compound was expected. The intermediate, 4-hydroxy-5-isopropyl-2-methylisophthalaldehyde, was synthesised *via* the hexamine aromatic formylation – *i.e.*, a Duff reaction – between thymol and urotropine and obtained without any column purification (Fig. 2 and Fig. S1, S2, ESI†).[40] Subsequently, the alcohol moiety underwent a nucleophilic substitution with 1-(2-bromoethoxy)-2-(2-methoxyethoxy)-ethane (Br-TEG) to improve the solubility of the monomer in water (Fig. 1B, R_2). Furthermore, Br-TEG presents no acute toxicity compared to methyl iodide, which we previously used in the nucleophilic substitution reaction with the alcohol group.[25] ^{1}H, ^{13}C NMR, and LC-MS confirmed the successful formation of the AA monomer (Fig. 2B and Table S1, Fig. S3–S5, ESI†). A commercially available bismaleimide counterpart (2,4 toluene bismaleimide, BB1, Table S2 and Fig. S6, S7, ESI†) was used to screen various particle formation parameters, whilst a degradable bismaleimide (bis(2,6-dichloro-4-*N*-maleimido) phenyl) oxalate, (BB2) was employed to produce degradable chemiluminescent particles. We synthesised BB2 in accordance with previously reported procedures and characterised accordingly (Table S3 and Fig. S8, S9, Scheme S4, ESI†).[35]

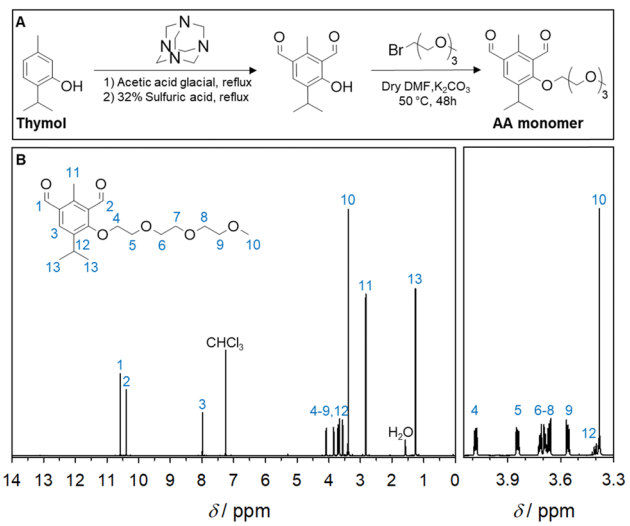

Fig. 2 (A) Synthetic route for the AA monomer (5-isopropyl-4-(2-(2-(2-methoxy ethoxy)ethoxy)ethoxy)-2-methylisophthalaldehyde). Thymol is first stirred in glacial acetic acid at 115 °C for 12 h, 33% H_2SO_4 is added, and the reaction stirred at 100 °C for 12 h. Br-TEG is then added in dry DMF, with K_2CO_3 and heated at 50 °C for 48 h. (B) ^{1}H NMR of the AA monomer.

Photoflow synthesis of the nanoparticles

In photochemistry, light penetration depth, the absorption of light by chromophores, the influence of light scattering by particles, concentration and the distance between the light source and the reaction (path length) are critical, as specified by Beer–Lambert's law.

Therefore, photochemical reactions – and more specifically photo-polymerisations in dispersed media – are limited in batch reactions and are difficult to scale-up due to light penetration issues, reducing efficiency. As noted, flow reactors can help circumvent these problems. The small diameter tubing is in close proximity to the light source which evenly irradiates the reaction medium and the continuous flow of reagents allows for, in principle, unlimited synthesis of product (providing there is unlimited feedstock).[28]

In precipitation polymerisations, acetonitrile (ACN) is commonly chosen as the θ-solvent.[4] Therefore, we initially prepared an equimolar 10 mmol L^{-1} stock solution of AA and BB1 monomers in acetonitrile (Fig. 3). We chose this concentration as a compromise based upon existing microsphere synthesis routes that used 5 mmol L^{-1} and 20.0 mmol L^{-1}.[24,25] The equimolar ratio was confirmed by ^{1}H NMR spectroscopy (Fig. S10, ESI†). The stock solution was continuously pumped at 0.5 mL min^{-1} through a flow reactor (refer to the experimental section for technical specifications) equipped with eight 2 W (16 W in total), 365 nm LED lamps *via* a 1.3 mm diameter tubing (Fig. S11 and S12, ESI†) (Experiment 1).

It should be noted that, whilst the stock solution of starting reagents was clear and homogeneous, the solution became turbid after passing through the photoflow reactor, indicating particle formation. The particles were readily recovered *via* centrifugation and decanting off the solution. The residual reaction mixture (supernatant) was collected and analysed later, as it contains a mixture of unreacted monomers and soluble, unprecipitated oligomers. The solvent was removed *in vacuo*, and the supernatant was subsequently weighed and analysed by size exclusion chromatography (SEC). Here, a yield of 1% (calculated from the mass of particles recovered, as explained in the Experimental section below) was recovered and was qualitatively analysed by SEM (Fig. S13, ESI†). The SEM images show particles with a mean diameter of 730 nm ($Đ$ = 0.039). Following the initial experiment in acetonitrile, we determined the best solvent for the reaction before optimising the photochemical flow synthesis. Therefore, we analysed the recovered particle mass and imaged the particles by SEM, to obtain qualitative and quantitative information about the particles formed.

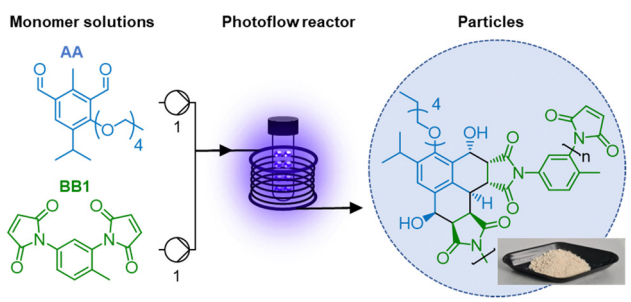

Fig. 3 An equimolar solution of AA and BB monomer are fed into a photoflow reactor to yield particles *via* a Diels–Alder step-growth polymerisation.

We subsequently investigated acetone as reaction solvent (Experiment 2), as reported by Kammerer *et al.* in the synthesis of similarly structured polyaromatic microparticles in a batch process;[24] however, in this instance, no particle formation was observed. Our attention then turned to water, as we hypothesised that the triethylene glycol chain on the AA monomer should increase water solubility. Unfortunately, solubility issues, particularly surrounding the insolubility of monomer BB1 prevented the use of pure water. We therefore investigated combinations of organic solvents with water. Acetonitrile and water (1 : 1) resulted in particle formation, with a yield of 10% recovered (Experiment 3). SEM imaging confirmed the successful formation of particles with a mean diameter of 565 nm ($Đ$ = 0.04) (Fig. S14, ESI†). Nevertheless, we noted some evidence of blocks of oligomer and particles adhering to each other due to residual unwashed oligomer. The combination of acetone and water (1 : 1) resulted in the highest particle yield of 39% (Experiment 4). SEM imaging showed particles with a mean diameter of 268 nm ($Đ$ = 0.012), with little oligomer present and no cementing of particles (Fig. S15, ESI†). SEM analysis thus revealed that the particles produced in acetonitrile/water were smaller than those synthesised solely in acetonitrile, and the ones synthesised in acetone/water were even smaller. Since the θ-solvent directly influences the solubility, it appears that the growing polymer will precipitate earlier and form more nuclei and smaller particles with more hydrophilic solvent combinations. SEC analysis of the supernatant confirms this solubility trend with dissolved oligomers with molecular weights of up to 60 000, 10 000, and 6000 g mol^{-1} for acetonitrile, acetonitrile/water, and acetone/water, respectively (Fig. S16, ESI†). These molecular weights mark the solubility limits for the respective solvents and the degree of polymerisation necessary for particle precipitation. For the combination of acetone and water, the solubility drastically decreases for oligomers longer than 9 monomer units (Fig. S17, ESI†).

It is evident from these initial experiments that a combination of acetone and water yields a significantly higher nanoparticle yield (Fig. S18, ESI†). It is worth mentioning that a brief exploration of longer retention times was carried out (by passing the reaction solution multiple times through the flow reactor), which, in the case of some solvent combinations, did increase the mass of nanoparticles recovered. However, this process resulted in no significant advantage as it did not surpass the particle yield from passing the reaction mixture once through the flow reactor (at a flow rate of 0.5 mL min^{-1}, equating to a retention time of *ca.* 20 min) and the overall reaction time was significantly longer (*ca.* 3 h) (Fig. S19, ESI†). Therefore, these conditions were not explored further and in all subsequent experiments, the reagent mixture was passed once through the flow reactor whilst being irradiated.

Table 1 Overview of results obtained from varying the flow rate, whilst maintaining a concentration of 10 mmol L^{-1} in 1 : 1 acetone : water. See Fig. 5 for graphical representation

Experiment number	Flow rate/mL min^{-1}	Retention time/min′s″	Particle yield/%	Mean apparent diameter $\bar{d}$/nm	Dispersity $Đ$	Mean roundness
5	0.10	60′00″	61	313	0.084	0.98
6	0.30	29′45″	63	276	0.033	0.94
7	0.50	16′55″	47	268	0.012	0.97
8	0.70	10′50″	50	255	0.040	0.94
9	0.80	8′25″	54	255	0.026	0.95
10	0.90	7′40″	50	251	0.030	0.94
11	1.00	6′55″	46	250	0.033	0.95
12	1.20	5′30″	38	257	0.028	0.94
13	1.50	6′40″	30	261	0.026	0.91
14	2.00	4′30″	25	240	0.022	0.89
15	2.50	3′35″	10	185	0.028	0.98
16	5.00	2′00″	17	193	0.033	0.83

Next, with the 1 : 1 solvent mixture of acetone and water selected, other parameters were altered to investigate their effect on yield, particle shape, diameter, and dispersity. Firstly, the effect of flow rate was explored, with experiments carried out at specific intervals from 0.1 mL min^{-1} to 5.0 mL min^{-1} (Table 1). A concentration of 10 mmol L^{-1} was selected, as per Experiments 1–4 described above. In each case, the retention time of the reaction mixture in the flow reactor and the particle yield (calculated from the volume collected and mass of particles recovered, refer to Table S4 (ESI†) and the experimental section below) were recorded. The resulting nanoparticles were subsequently analysed by SEM (as visually depicted by the SEM images in Fig. 4), which gave further information about the particles' diameter, dispersity and roundness. The SEM images indicate that in all cases there was dispersity in size and variations in roundness. The particles were counted using the ImageJ software,[41] which enabled us to quantify size, dispersity and roundness, and analyse them statistically (refer to Fig. S20 for an exemplary image analysis, and Fig. S21 and S22 for the full statistical analysis, ESI†). Since – depending on the experimental parameter – a larger or smaller fraction of particles appeared elliptical rather than round, we measured all particles as ellipses, calculated their volume, and back-calculated the apparent diameter for a round particle from this volume. Our approximation is valid, as the largest fraction of particles still displays a roundness close to 1 (refer to Fig. S22 and S28, ESI†), and still provides an intuitive measure for the size of the particles. The results of the statistical analysis are displayed in Table 1 and summarised graphically in Fig. 5, to visualise systematic trends. Except for 0.1 mL min^{-1}, the dispersity remains constant with increasing flow rate. At the same time, the apparent particle diameter decreased from 313 to 193 nm with increasing flow rate. Interestingly, we also visually observe that the roundness of the particles decreases as they seem to elongate into an elliptical shape with increased flow rate (Fig. 4). Since there are no additives or surfactants and precipitation polymerisation is sensitive to agitation, the solution in batch reactions is only stirred gently to prevent colloidal

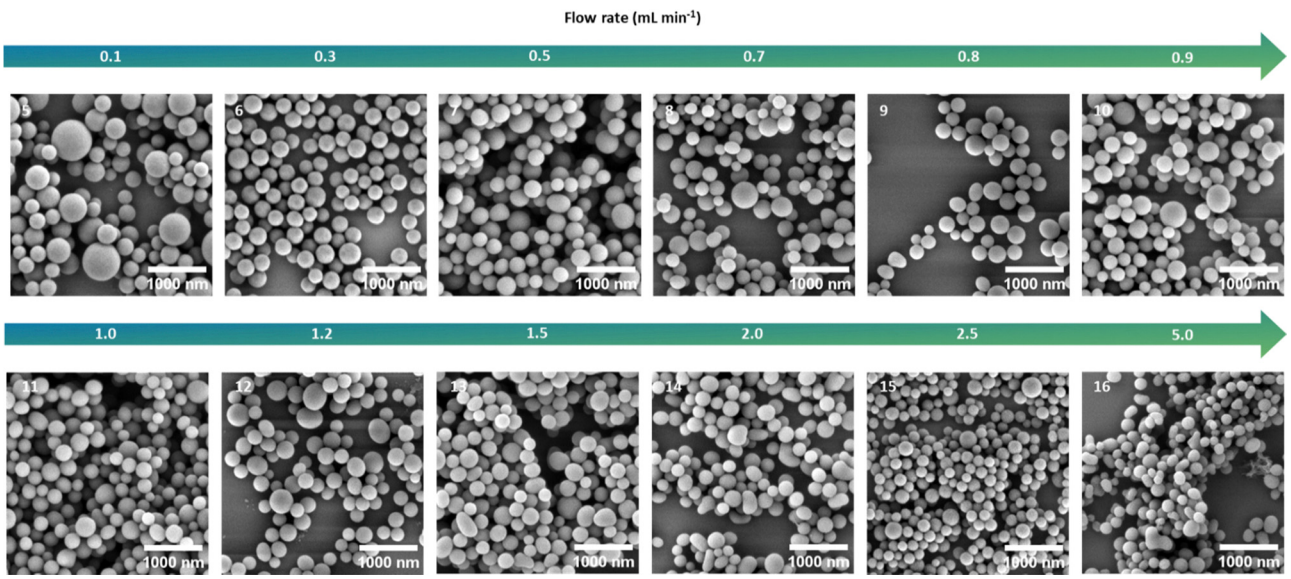

Fig. 4 SEM images of the isolated particles with increasing flow rate from left to right and top to bottom (experiments 5 – 16). [AA] = [BB] = 10 mM, 1 : 1 acetone : water.

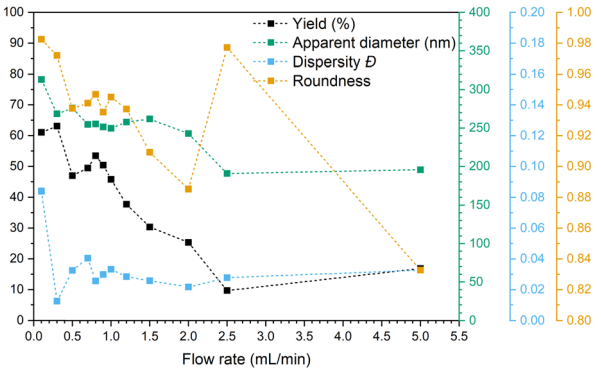

Fig. 5 Nanoparticle yield, apparent diameter, dispersity, and roundness when the flow rate is varied (experiments 5–16).

instability. In the case of flow synthesis, some agitation might be caused by the motion from the peristaltic pumps. Higher flow rates could thus impact the shape of the particles and the yield, which drastically decreased from 60 to 10%. However, a negative effect on precipitation by agitation would result in polymers with a higher molecular weight visible in the SEC chromatograms, as these would stay in solution. This was not observed, and the solubility limit remained constant at a molecular weight of 6000 g mol ^{1}, independent from the flow rate (see Fig. S17, ESI†). Only for the highest flow rate, the molecular weight distribution is significantly shifted to lower molecular weights, which is a result of the low conversion due to the short retention time. Thus, agitation has – within the tested range of flow rates – only a negative effect on the particle morphology but not on particle precipitation itself, and the observed lower particle yield is an effect of the lower conversions. Furthermore, we observe a strong correlation of yield and particle size with a correlation coefficient of 0.85 (Fig. S23, ESI†). The strong correlation between yield and particle diameter suggests that the yield mainly affects the particle growth and not particle nucleation, *i.e.*, the precipitation of more polymer results in larger, not more particles.

Based on the statistical analysis, we identified 0.8 mL min ^{1} as the optimal flow rate (refer to Fig. S24 for further SEM images, ESI†). 0.8 mL min ^{1} gave a high yield (>50%) at a tolerable retention time without being affected by the negative morphological impacts of faster flow rates. Since the particles are insoluble, we instead analysed the supernatant, as it can provide valuable insights into the polymer backbone. NMR analysis of the supernatant (Experiment 14) showed some residual AA monomer and trace amounts of BB (Fig. S25, ESI†). However, the spectrum clearly evidenced the OH and H resonances of the newly formed ring structures and confirmed the formation of the expected Diels–Alder photopolymer.

Subsequent experiments at the flow rate of 0.8 mL min ^{1} were carried out to observe the effect of varying the concentration (*cf.* Beer–Lambert's law). Concentrations of 2.5, 5.0, 10.0 and 15.0 mmol L ^{1} were investigated; the results of which are presented in Table 2. The stock solutions prepared were analysed by NMR spectroscopy to confirm equimolarity (Fig. S26 and Table S5, ESI†). Here it was observed that up until 10 mmol L ^{1}, the monomers remained in an equimolar ratio, yet beyond this the concentration began to influence the monomer solubility. 20.0 mmol L ^{1} was attempted, but the concentration was too high and further affected solubility and monomer equimolarity and caused blockages in the flow reactor tubing. The concentration variations showed that 10 mmoL L ^{1} seemed to give the highest particle yield (calculated from the volume collected and mass of particles recovered, see Table S6 and Experimental section below, ESI†) and lowest dispersity. The particles obtained at the different concentrations were also imaged by SEM (Fig. S27, ESI†). At a concentration of 15 mmol L ^{1}, the shape of the particles becomes distinctly deformed, as the equimolar ratio of AA to BB is no longer possible. The statistical analysis of the particle morphology is displayed in Table 2 and Table S6 (ESI†), and is summarised graphically in Fig. 6 (refer to Fig. S28 and S29 for the full statistical analysis, ESI†). Fig. 6 (and Fig. S27, ESI†) shows that at 15 mmol L ^{1}, the concentration is too high and results in poor particle formation. Whilst dispersity remains relatively constant for Experiments 17–19 (2.5–10 mmol L ^{1}), a slight decrease in roundness is observed. Experiment 19 exhibits the highest particle yield (>50%), indicating that 10 mmol L ^{1} appears to be the optimal concentration for the nanoparticle synthesis. It is worth noting, however, whilst the apparent diameter between 5.0 and 10.0 mmol L ^{1} seems to be fairly consistent, it is around 250 nm higher at a concentration of 2.5 mmol L ^{1}. Whilst interesting, apparent diameter on its own does not define successful micro- or nanoparticle formation but becomes relevant depending on the targeted application. Again, analysis of the supernatants by SEC shows only dimer and low-order oligomers (Fig. S30, ESI†).

Finally, a control experiment (Experiment 21) was conducted, whereby a 10 mmol L ^{1} stock solution of just AA monomer was prepared and passed through the flow reactor at 0.8 mL min ^{1}, irradiated at 365 nm. A completely homogeneous, clear yellow

Table 2 Overview of results obtained from varying the concentration in 1 : 1 acetone : water, whilst maintaining a constant flow rate of 0.8 mL min^{-1}. See Fig. 6 for graphical representation

Experiment number	Concentration/mmol L^{-1}	Retention time/ min′s″	Particle yield/ %	Mean apparent diameter $\bar{d}$/nm	Dispersity $Đ$	Mean roundness
17	2.5	10′10″	37	527	0.027	0.97
18	5.0	10′40″	48	274	0.032	0.97
19	10.0	8′25″	54	256	0.026	0.95
20	15.0	10′30″	47	281	0.056	0.92

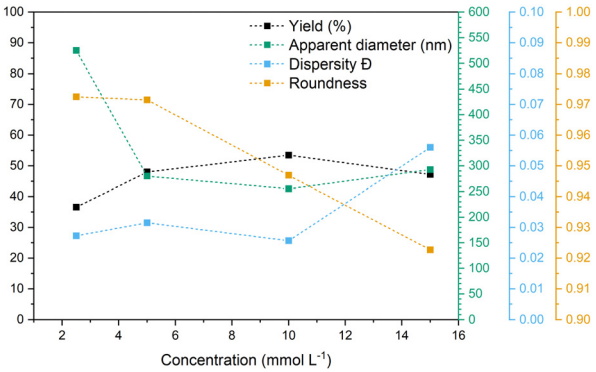

Fig. 6 Nanoparticle yield, apparent diameter, dispersity, and roundness when concentration is varied (experiments 17–20).

solution was obtained. SEM analysis of the crude reaction mixture obtained showed no evidence of particle formation. The solution was centrifuged at 9000 rpm for 5′30″, but no solid material precipitated from the solution, confirming that both the aldehyde and maleimide must be present to form particles, thus confirming the [4+2] cycloaddition that occurs during particle synthesis.

In summary, we have demonstrated the viability of the additive-free photoflow synthesis of polymer particles by precipitation polymerisation. Even though the exact mechanism of the additive-free precipitation of particles is yet to be revealed and part of an ongoing investigation, we identified the influence of various reaction parameters on the nucleation and growth behaviour of the particles. The choice of solvent determines the solubility of the photopolymer and thus significantly influences the maximum molecular weight before precipitation as well as the nucleation behaviour. A good solvent (*e.g.* acetonitrile) leads to higher critical molecular weights for precipitation as well as larger particles. A poorer solvent (*e.g.* a mix of acetone and water) leads to lower critical molecular weights for precipitation and smaller particles at higher overall yields. The larger number of particles at higher yields highlights the increased nucleation of particles within a worse solvent due to reduced solubility as the driving force. For the same solvent, the particle size and yield are strongly correlated, indicating that a higher yield leads to more particle growth rather than increased nucleation. Agitation as a result of the flow only effects the particle shape and not the amount of precipitated polymer within the investigated flow rates of up to 5 mL min^{-1} and the used flow reactor.

Reaction upscaling and Brunauer–Emmett–Teller (BET) analysis

With the optimum flow rate and concentration of 0.8 mL min^{-1} and 10 mmoL L^{-1} chosen respectively, the photoflow reaction was significantly upscaled with a view to producing over 0.5 g for BET analysis. This also demonstrates the potential of this technique for further upscaling. In principle, with more stock solution, this continuous method would enable the synthesis of a greater quantity of particles and overcome the constraints imposed by the size limitations of available glassware. As the yield from 0.5 g synthesis is comparable to the smaller-scaled reactions reported in Tables 1 and 2, it suggests that upscaling has limited impact on efficiency and yield. Therefore, 0.545 g (yield = 48%) was recovered and analysed by BET (Fig. S31–S33, ESI†). BET analysis is a standard method to determine the specific surface area of a material by measuring its N_2 adsorption at varying pressures. BET provides insights into the material's morphology and porosity, as the gas also adsorbs at the surface of internal pores. The BET surface area measured was 14 m^2 g^{-1} and showed no evidence of the existence of micropores or small mesopores. As a comparison, porous polymeric particles present surface area generally above 100 m^2 g^{-1} up to 800 m^2 g^{-1}.[42]

Chemiluminescent read-out

After successfully demonstrating the implementation of photoflow chemistry to produce particles within minutes, we explored the potential of our particles for point-of-care devices with a straightforward output, namely light emission. Thus, we substituted monomer BB1 with a peroxyoxalate-containing BB monomer (BB2). For solubility reasons, the reaction was conducted in acetonitrile at a concentration of 2.5 mmol L^{-1} and a flow rate of 0.5 mL min^{-1}, similar to Experiment 1. We successfully synthesised particles with an AA + BB2 backbone (Experiment 22, Fig. 7A). SEM analysis indicated a particle size of 715 nm with a dispersity of 0.03 (Fig. 7B and Fig. S34, ESI†). The supernatant was also analysed by SEC (Fig. S35, ESI†), showing again dimer and low-order oligomers up to 3000 g mol^{-1} present. Notably, the Diels–Alder adduct exhibited intrinsic fluorescence, serving as a fluorophore for the peroxyoxalate chemiluminescent reaction. Upon introducing hydrogen peroxide – capable of cleaving the oxalate bond and exciting the fluorophore – photons were emitted, peaking at 4×10^5 counts after a few minutes (Fig. S36, ESI†). In contrast, without hydrogen peroxide, no chemiluminescence occurred, and the instrument recorded a baseline of 5×10^2 counts. As shown in Fig. S37 (ESI†), the emitted light peaked at 520 nm in the blue region. Subsequent SEM analysis following the addition of hydrogen peroxide confirmed the particle degradation resulting from the cleavage of the oxalate bond, wherein macromolecular chains formed a polymeric layer (Fig. 7C and Fig. S38, ESI†). Recognising the potential of our material for sensing applications due to its distinct photon response to the introduction of hydrogen peroxide, we proceeded to dilute the particle concentrations in the solution. At a concentration of 0.3 mg mL^{-1}, the light output was measured at 8×10^3 counts, which is 17 times higher than the baseline. The light output consistently increased with higher concentrations up to 4×10^5 at 1 mg mL^{-1} (Fig. 7D and Table S7, ESI†). These experiments clearly demonstrate a direct correlation between the particles and the emitted light.

Conclusions

We introduce an industrially relevant approach to synthesise polymeric nanoparticles. Our approach is additive-, radical-, and

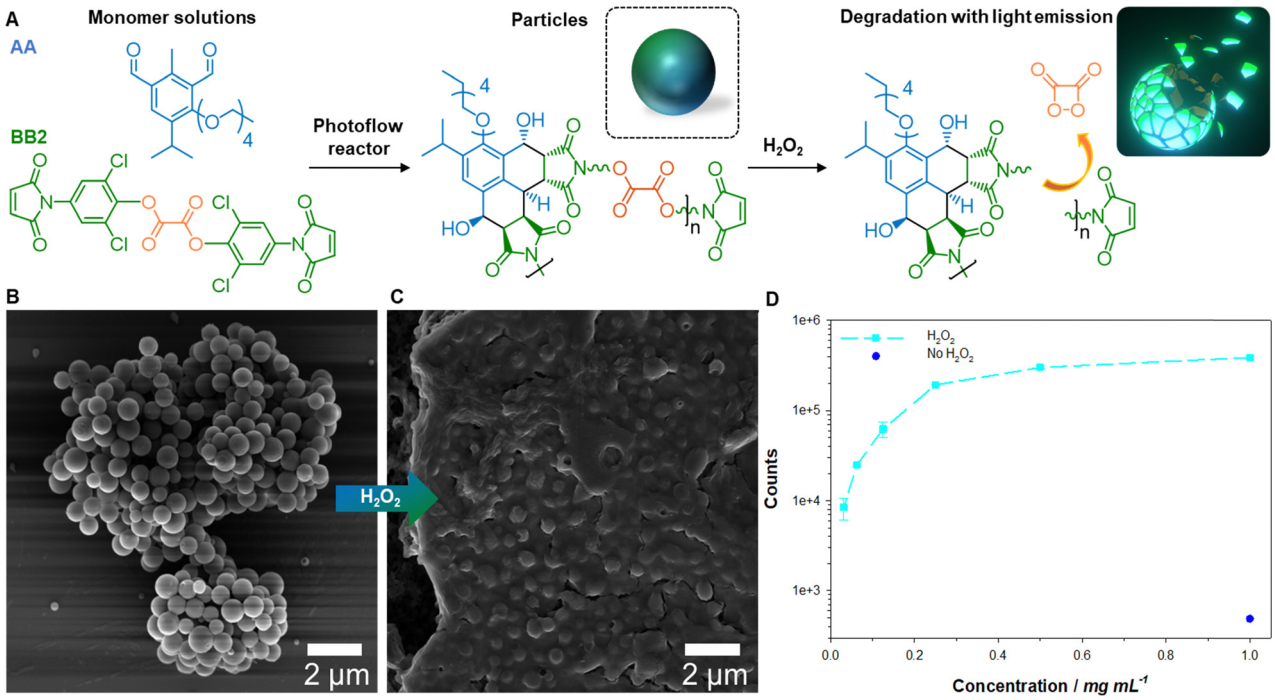

Fig. 7 (A) Overview of the particle formation with AA and BB2 monomers and subsequent cleavage of the oxalate bond in presence of H_2O_2, resulting in the degradation of the particles and light emission. (B) SEM image of the particles after synthesis. (C) SEM image of the particles after adding H_2O_2. (D) Photocount recorded at various particles concentrations.

surfactant-free and proceeds under ambient conditions, using irradiation by LED to initiate the reaction. We further base our nanoparticle synthesis on a sustainable starting reagent derived from a natural product, requiring no highly toxic methylating agents. We demonstrate the capability of using continuous flow chemistry, rather than the previously reported batch synthesis technique, in combination with UV-light irradiation to synthesise nanoparticles on larger scales and in a relatively short timeframe, thus offering a significant improvement compared with batch synthesis, which can take several hours.

We underpin our innovation by a comprehensive study, investigating the variation of the main parameters of flow synthesis, namely flow rate, concentration, and solvent composition, with regards to nanoparticle formation, demonstrating that we can optimise nanoparticle photoflow synthesis for yield, roundness, dispersity, and particle size. Moreover, we were able to unravel the influences of said experimental parameters on the nucleation and growth of the particles and effectively demonstrate the potential of continuous flow synthesis by synthesising more than 0.5 g of nanoparticles. Having demonstrated the translation of effective light-driven particle production in flow on the laboratory scale, we submit that the prospects of constructing a larger-scale flow reactor which utilises sunlight, thus exploiting photons as a free and traceless reagent, is an enticing future proposition, particularly under the high photon flux conditions of our home continent, Australia.

Finally, the introduction of chemiluminescence through careful monomer design – which also introduced degradability upon the addition of hydrogen peroxide – effectively demonstrates the potential of these materials in applications such as point-of-care devices. Therefore, the easy and up-scalable synthesis approach in combination with the ability to synthesise structures which are degradable with visual feedback highlights real-world and industrial potential.

Experimental

Materials

All materials were reagent grade and used as received, unless stated otherwise: 2-isopropyl-5-methylphenol (≥98.5%, Sigma-Aldrich), hexamethylenetetramine (≥99.5%, Sigma-Aldrich), sulfuric acid (96%, Thermo-Fischer), hydrochloric acid (32%, Thermo-Fisher), 2-[2-(2-methoxyethoxy)ethoxy]ethyl bromide (97%, Combi-blocks), acetic acid (glacial) (Thermo-Fisher), oxalyl chloride (Sigma-Aldrich, ≥99%) potassium carbonate (99.9%, Merck), triethylamine (Sigma-Aldrich, ≥99.5%), 2,4-toluene bismaleimide (Evonik), 4-amino-2,6-dichlorophenol (98%, Combi-blocks), maleic anhydride (99%, Sigma-Aldrich), *N*,*N*′-dimethylformamide, anhydrous (DMF, 99.8% Sigma-Aldrich) ethyl acetate, anhydrous (Sigma-Aldrich, 99.8%) *N*,*N*′-dicylohexylcarbodiimide (DCC) (Sigma-Aldrich), magnesium sulphate, anhydrous (Merck), acetonitrile (ACN, HPLC-grade, Thermo-Fisher), dimethyl sulfoxide (DMSO, analytical reagent, Thermo-Fisher), acetone (analytical reagent, Thermo-Fisher), methanol (MeOH, analytical reagent, Ajax Finechem), tetrahydrofuran (THF, 99.8% analytical reagent, Fisher), cyclohexane

(CH, analytical reagent, Ajax Finechem), ethyl acetate (EA, analytical reagent, Thermo-Fisher), dichloromethane (DCM, analytical reagent, Thermo-Fisher), *n*-pentane (analytical reagent, Thermo-Fisher), acetonitrile-d_3 (ACN-d_3, 99.8%D, Cambridge Isotope Laboratories), chloroform-*d* ($CDCl_3$, 99.8%D, Cambridge Isotope Laboratories), dimethylsulfoxide-d_6 (DMSO-d_6, 99.9%D, Cambridge Isotope Laboratories), tetrahydrofuran-d_8 (THF-d_8, 99.5%D, Cambridge Isotope Laboratories).

Methods

Flow reactor (refer to Fig. S11 for images, ESI†). A Vapourtec E2 Flow Reactor was used to perform photoreactions under flow conditions. The Vapourtec E-series device was equipped with peristaltic pumps in combination with the UV-150 module and the VSD006 cooling module. The module consists of a temperature-controlled irradiation chamber, a transparent fluorinated ethylene polymer (FEP) reactor coil (1.3 mm inner diameter, 0.15 mm wall thickness, total volume = 10 mL) and a standard LED assembly (Gen-2, 360 to 390 nm, peak 365 nm, total power output of 16 W). The temperature is controlled by pre-cooled (using liquid N_2) nitrogen (heat exchange in the cooling module).

Scanning electron microscopy (SEM). SEM images were captured using a Tescan MIRA3 using an in-lens, in-beam secondary electron (SE) detector at a 2.5–3 mm working distance and 2–3 kV acceleration voltage (beam intensity = 6), depending on charging observed. Samples were prepared by dispersing the particles in methanol and drop casting onto a silicon wafer glued onto a SEM stub using conductive carbon tape. Samples were coated with a 3 nm platinum layer. Analysis was conducted using ImageJ, counting a minimum of 300 particles. Since the particles formed depending on the experimental parameter ellipses rather than spheres, we used the apparent diameter as a uniform and intuitive measure for the particle size. Therefore, we measured all particles as ellipses, calculated their volume, *V*, according to

$$V = \frac{4}{3}\pi a b^2.$$

Thereby is *a* the long axis and *b* the short axis of the ellipse. We then back calculated the apparent diameter *d* of a sphere from this particle volume according to

$$d = 2 \cdot \sqrt[3]{\frac{3}{4\pi}V}.$$

We calculated the dispersity of the particles according to[43]

$$Đ = \left(\frac{\sigma}{\bar{d}}\right)^2$$

Where $\bar{d}$ is the mean particle diameter and σ its standard deviation. The roundness *R* was calculated as the inverse aspect ratio of the ellipses with

$$R = \frac{a}{b}$$

Please refer to the ESI,† for details of further methods used (nuclear magnetic resonance spectrometry (NMR), liquid chromatography coupled mass spectroscopy (LC-MS), flash chromatography, centrifugation, Brunauer–Emmett–Teller (BET), and chemiluminescence measurements).

Monomer synthesis

Synthesis of 4-hydroxy-5-isopropyl-2-methylisophthalaldehyde (Scheme S1, ESI†). 2-Isopropyl-5-methylphenol (8.00 g, 53.25 mmol, 1 eq.) and hexamethylenetetramine (7.47 g, 53.25 mmol, 1 eq.) were dissolved in acetic acid (200 mL) (Scheme S1, ESI†). The solution was stirred and heated to 115 °C and allowed to reflux overnight under argon atmosphere. The reaction mixture was cooled to ambient temperature, and 33% sulfuric acid (267 mL) was added. The reaction mixture was heated to 60 °C overnight. The reaction mixture was again cooled to ambient temperature. The dark brown solution was extracted twice with pentane (2 × 300 mL). The organic layers were combined and washed with water, dried over magnesium sulphate and filtered. The solvent was evaporated *in vacuo* and dried overnight on the Schlenk line. A yellow solid was obtained as the final product. Yield = 37% (4.048 g). ^{1}H NMR (600 MHz, $CDCl_3$): δ = 13.10 (s, 1H), 10.48 (s, 1H), 10.26 (s, 1H), 7.92 (s, 1H), 3.34 (hept, J = 6.9 Hz, 1H), 2.92 (s, 3H), 1.25 (d, J = 7.1 Hz, 6H) (Fig. S1, ESI†).

^{13}C (151 MHz, $CDCl_3$): δ = 195.95, 190.43, 165.95, 144.33, 136.48, 136.24, 126.59, 118.12, 26.52, 22.58, 12.28. (Fig. S2, ESI†).

Synthesis of 5-isopropyl-4-(2-(2-(2-methoxyethoxy)ethoxy) ethoxy)-2-methylisophthalaldehyde (Scheme S2, ESI†). 4-Hydroxy-5-isopropyl-2-methylisophthalaldehyde (4.048 g, 19.63 mmol, 1 eq.,) was dissolved in anhydrous DMF (120 mL) under an inert atmosphere. 2-[2-(2-methoxyethoxy)ethoxy]ethyl bromide (Br-TEG) (7.92 mL, 31.99 mmol, 1.63 eq.) was added to the reaction mixture dropwise. Potassium carbonate (3.34 g, 24.14 mmol, 1.23 eq.) was added to the reaction mixture, which was then purged with nitrogen for 15 minutes. The reaction mixture was heated to 50 °C for 72 hours. (Scheme S2, ESI†) After cooling to ambient temperature, hydrochloric acid (200 μL, 2 M) was added to the reaction mixture. The reaction was filtered, and the solvent evaporated *in vacuo*. The crude product was optionally dissolved in a mixture of water and DMSO and freeze-dried to remove excess Br-TEG. The product was then purified *via* automated column chromatography (EtOAc:CH 0:100-20:80 v/v). This was repeated, if required, to remove any residual impurity. The final produced was obtained as a yellow oil. Yield = 38% (2.616 g). Overall yield = 13.9%. ^{1}H NMR (600 MHz, $CDCl_3$): δ = 10.58 (s, 1H), 10.39 (s, 1H), 7.99 (s, 1H, H6), 4.10–4.06 (t, 2H), 3.86–3.82 (t, 2H), 3.73–3.64 (m, 6H), 3.58–3.54 (t, 2H), 3.44–3.35 (t, 1H), 3.37 (s, 3H), 2.83 (s, 3H), 1.26 (dd, J = 6.9, 1.0 Hz, 6H). (Fig. S3, ESI†).

^{13}C NMR (151 MHz, $CDCl_3$) δ 193.23, 190.70, 164.13, 141.43, 140.83, 133.59, 131.47, 129.39, 128.65, 76.30, 71.78, 70.74, 70.51, 70.47, 69.87, 58.81, 25.64, 23.32, 13.94 (Fig. S4, ESI†).

LC-MS *m*/*z*: $[C_{19}H_{28}O_6]^+$ calculated for $C_{19}H_{28}O_6^+$, 353.1959; found, 353.1956. $[C_{19}H_{28}O_6]NH_4^+$ calculated for $C_{19}H_{28}O_6NH_4^+$, 370.2224; found, 370.2218 (Table S1 and Fig. S5, ESI†).

Synthesis of (bis(2,6-dichloro-4-*N*-maleimido)phenyl) oxalate (BB2). (Scheme S3, ESI†)[35]. 4-Amino-2,6-dichlorophenol

(1.00 g, 5.6 mmol, 1 eq.) was dissolved in acetone (20 mL). Maleic anhydride (660 mg, 6.7 mmol, 1.2 eq.) was dissolved in acetone (5 mL) and was added dropwise. The reaction was stirred for 1 hour under ambient conditions until a yellow precipitate formed. The solid was filtered off and washed with acetone. 500 mg of the resulting solid was dispersed in dichloromethane (20 mL). To this, *N*,*N*′-dicyclohexylcarbodiimide (DCC) (720 mg, 3.4 mmol, 1.2 eq.) was added portion wise and the reaction heated to reflux overnight. The precipitate was then filtered off and washed with dichloromethane. The filtrate was evaporated (without heating), and the residual product was redissolved in acetonitrile. The formed precipitate was filtered off and washed with acetonitrile. The filtrate was evaporated, and the residual product was redissolved in and washed with cold methanol. A yellow solid of 1-(3,5-dichloro-4-hydroxyphenyl)-1*H*-pyrrole-2,5-dione was obtained. Yield = 75% (348 mg).

165 mg of this product (0.64 mmol, 1.0 eq.) was dissolved in anhydrous ethyl acetate (15 mL). 3 Å molecular sieves were added and the reaction was de-gassed for 15 minutes with argon. Triethylamine (133.7 μL, 0.96 mmol, 1.5 eq.) was added. The reaction was cooled with an ice bath. Oxalyl chloride (41.1 μL, 0.48 mmol, 0.75 eq.) was solubilised in anhydrous ethyl acetate (2 mL) and added dropwise to the reaction. The reaction was stirred for a further 30 minutes on an ice bath and then for a further 1.5 hours at room temperature. The solvent was then removed *in vacuo* (without heating). The resulting solid was dispersed in methanol, filtered off and washed with small amounts of methanol and ethyl acetate so that a colourless solid remained. Yield = 36.5% (133 mg). The product was characterised in accordance with the literature (Fig. S8, S9 and Table S3, ESI†).

Particle synthesis

A 10 mmol L $^{-1}$§ equimolar stock solution of the AA and BB1 monomer was prepared in solvent,§ in amber glassware. The solution was then passed through a 2.5 μm PTFE syringe filter and then de-gassed with argon for at least 10 minutes. The flow reactor was flushed with water. Afterwards, the stock solution was sent through the flow coil at a constant temperature of 20 °C at a flow rate ranging from 0.10 to 5.0 mL min $^{-1}$§, irradiated at 365 nm (16 W) and collected in a pre-weighed centrifuge tube. The volume collected ($V_{collected}$) was noted and used for the yield calculations. As we observed that particles could be stuck within the tube, the flow reactor was subsequently purged (without irradiation) with 5 mL of water at 5.0 mL min $^{-1}$, which was also collected in the pre-weighed centrifuge tube. The turbid solution was centrifuged§, then the supernatant was decanted into a pre-weighed round bottom flask, and the solid pellet was washed with 25 mL of THF (solution was sonicated until well dispersed) and then centrifuged.§ The THF solution was decanted off into the pre-weighed round bottom flask with the rest of the supernatant. The resulting particles were redispersed in methanol (10 mL) and 10 μL was drop cast for SEM analysis. The methanol was subsequently evaporated, and the particles dried in an oven at 40 °C to determine the mass. Similarly, the solvent was removed *in vacuo* from the supernatant, and the residue was subsequently dried in the oven at 40 °C to determine the mass.

Yield calculations

For Experiments 1–4, the particle yields were calculated as follows:

$$\text{Yield} = \left({m_{\text{particles}}}/{m_{\text{particles}} + m_{\text{supernatant}}}\right) \times 100$$

$m_{particles}$ = mass of particles recovered, $m_{supernatant}$ = mass of supernatant recovered

For Experiments 5–20, the yield of the particles, which represents the conversion of monomer to particle, was calculated as follows:

$$m_{\text{start}} = m_{\text{AA}} + m_{\text{BB}}$$

m_{start} = total mass of start materials,
m_{AA} = mass of AA monomer
m_{BB} = mass of BB monomer

The proportion of the volume of solution collected after irradiation, compared with the total amount of stock solution prepared was used to calculate the expected total mass of nanoparticles (no mass loss was anticipated as this is a cycloaddition reaction):

$$x = \frac{V_{\text{stock}}}{V_{\text{collected}}}$$

V_{stock} = volume of stock solution (mL)
$V_{collected}$ = volume of reaction solution collected

$$m_{\text{theoretical}} = \frac{m_{\text{start}}}{x}$$

The yield could then be calculated as follows:

$$\text{Yield}\,(\%) = \left(\frac{m_{\text{particles}}}{m_{\text{theoretical}}}\right) \times 100$$

Author contributions

All authors contributed to the discussion and evaluation of the results at all stages. C. B.-K. and L. D. motivated, conceptualised, designed, and supervised the study. E. M. C. synthesised the monomer, J. O. H. synthesised the particles in flow and performed the SEM analyses, J. A. K. analysed the SEM data. L. D. performed the chemiluminescent experiments. L. D. and J. O. H. wrote the manuscript draft, which J. A. K., E. M. C. and C. B.-K. subsequently edited and refined.

Conflicts of interest

There are no conflicts to declare.

Acknowledgements

C. B.-K. acknowledges the Australian Research Council (ARC) for funding in the form of a Laureate Fellowship (FL170100014) underpinning his photochemical research program, as well as continued key support from the Queensland University of Technology (QUT) through the Centre for Materials Science. C. B.-K. and L. D. acknowledge funding in the context of an ARC Discovery grant focused on light-driven particle synthesis (DP230100445). J. A. K. is supported by the Deutsche Forschungsgemeinschaft (DFG, German Research Foundation) with a WBP fellowship—500289223. This work was enabled by use of the Central Analytical Research Facility (CARF) at the Queensland University of Technology (QUT). The authors thank Dr Jayanti Mendhi (QUT) for her assistance and advice on coating and analysis of the SEM samples.

References

§ Please refer to the ESI,† for details of each experiment (flow rate, concentration, centrifugation speed and time).

1 Y. Wang, L. Bao, J. Sun, Y. Ding, J. Shi, Z. Duan and Z. Chen, *J. Chromatogr. A*, 2022, **1680**, 463428.
2 O. O. Daramola, P. Adara, B. O. Adewuyi, E. R. Sadiku and W. K. Kupolati, in *Polymeric Biomaterials for Healthcare Applications*, ed. K. Varaprasad, Woodhead Publishing, 2022, ch. 3, pp. 71–123.
3 E. Campos, J. Branquinho, A. S. Carreira, A. Carvalho, P. Coimbra, P. Ferreira and M. Gil, *Eur. Polym. J.*, 2013, **49**, 2005–2021.
4 S. Pardeshi and S. K. Singh, *RSC Adv.*, 2016, **6**, 23525–23536.
5 J. P. Rao and K. E. Geckeler, *Prog. Polym. Sci.*, 2011, **36**, 887–913.
6 C. I. C. Crucho and M. T. Barros, *Mater. Sci. Eng., C*, 2017, **80**, 771–784.
7 R. Zhang, R. Gao, Q. Gou, J. Lai and X. Li, *Polymers*, 2022, **14**, 1851.
8 S. Khan, J. Vega-Chacón, G. A. Ruiz-Córdova, C. Pizan-Aquino, E. E. J. Jara-Cornejo, S. E. Torres, C. Jacinto-Hernández, R. López, M. D. P. T. Sotomayor, G. Picasso and J. E. L. Villa, in *Smart Polymer Nanocomposites*, ed. N. Ali, M. Bilal, A. Khan, T. A. Nguyen and R. K. Gupta, Elsevier, 2023, ch. 5, pp. 121–139.
9 C. H. Bamford, A. Ledwith and P. K. S. Gupta, *J. Appl. Polym. Sci.*, 1980, **25**, 2559–2566.
10 M. Yoshida, M. Asano, I. Kaetsu and Y. Morita, *Int. J. Radiat. Appl. Instrum., Part C*, 1987, **30**, 39–45.
11 J. S. Downey, R. S. Frank, W.-H. Li and H. D. Stöver, *Macromolecules*, 1999, **32**, 2838–2844.
12 G. L. Li, H. Möhwald and D. G. Shchukin, *Chem. Soc. Rev.*, 2013, **42**, 3628–3646.
13 M. G. Zolotukhin, V. G. Kozlov, Y. L. Sorokina, E. A. Sedova, K. V. Nefedjev and N. G. Gileva, *Angew. Chem., Int. Ed. Engl.*, 1993, **212**, 1–12.
14 M. G. Zolotukhin, D. R. Rueda, F. J. Balta Calleja, M. E. Cagiao, M. Bruix, E. A. Sedova and N. G. Gileva, *Polym.*, 1997, **38**, 1471–1476.
15 X. Gu, H. Sun, X. Kong, C. Fu, H. Yu, J. Li and J. Wang, *Colloid Polym. Sci.*, 2013, **291**, 1771–1779.
16 F. Limé and K. Irgum, *Macromolecules*, 2007, **40**, 1962–1968.
17 F. Limé and K. Irgum, *Macromolecules*, 2009, **42**, 4436–4442.
18 T. C. Bicak, *Macromol. Chem. Phys.*, 2021, **222**, 2100022.
19 T. C. Bicak, M. Garnier, M. Sabbah and N. Griffete, *Macromol. Rapid Commun.*, 2023, **44**, 2200966.
20 J. P. Hooker, L. Delafresnaye, L. Barner and C. Barner-Kowollik, *Mater. Horiz.*, 2019, **6**, 356–363.
21 J. P. Hooker, F. Feist, L. Delafresnaye, L. Barner and C. Barner-Kowollik, *Adv. Funct. Mater.*, 2019, 1905399.
22 J. P. Hooker, F. Feist, L. Delafresnaye, F. Cavalli, L. Barner and C. Barner-Kowollik, *Chem. Commun.*, 2020, **56**, 4986–4989.
23 C. W. Schmitt, S. L. Walden, L. Delafresnaye, H. A. Houck, L. Barner and C. Barner-Kowollik, *Polym. Chem.*, 2021, **12**, 449–457.
24 J. A. Kammerer, F. Feist, D. Ryklin, A. Sarkar, C. Barner-Kowollik and R. R. Schröder, *Adv. Mater.*, 2023, **35**, 2211074.
25 L. Delafresnaye, F. Feist, J. P. Hooker and C. Barner-Kowollik, *Nat. Commun.*, 2022, **13**, 5132.
26 M. B. Plutschack, B. Pieber, K. Gilmore and P. H. Seeberger, *Chem. Rev.*, 2017, **117**, 11796–11893.
27 M. Van De Walle, K. De Bruycker, J. P. Blinco and C. Barner-Kowollik, *Angew. Chem., Int. Ed.*, 2020, **59**, 14143–14147.
28 N. Zaquen, M. Rubens, N. Corrigan, J. Xu, P. B. Zetterlund, C. Boyer and T. Junkers, *Prog. Polym. Sci.*, 2020, **107**, 101256.
29 F. Jasinski, E. Lobry, A. Chemtob, C. Croutxé-Barghorn and A. Criqui, *Macromol. Chem. Phys.*, 2013, **214**, 1669–1676.
30 F. Jasinski, P. B. Zetterlund, A. M. Braun and A. Chemtob, *Prog. Polym. Sci.*, 2018, **84**, 47–88.
31 J. Wang, X. Hu, N. Zhu and K. Guo, *J. Chem. Eng.*, 2021, **420**, 127663.
32 N. Zaquen, J. Yeow, T. Junkers, C. Boyer and P. B. Zetterlund, *Macromolecules*, 2018, **51**, 5165–5172.
33 M. Yang, J. Huang, J. Fan, J. Du, K. Pu and X. Peng, *Chem. Soc. Rev.*, 2020, **49**, 6800–6815.
34 L. Delafresnaye, F. R. Bloesser, K. B. Kockler, C. W. Schmitt, I. M. Irshadeen and C. Barner-Kowollik, *Chem. – Eur. J.*, 2020, **26**, 114–127.
35 L. Delafresnaye, C. W. Schmitt, L. Barner and C. Barner-Kowollik, *Chem. – Eur. J.*, 2019, **25**, 12538–12544.
36 V. X. Truong, J. O. Holloway and C. Barner-Kowollik, *Chem. Sci.*, 2022, **13**, 13280–13290.
37 L. Delafresnaye, J. P. Hooker, C. W. Schmitt, L. Barner and C. Barner-Kowollik, *Macromolecules*, 2020, **53**, 5826–5832.
38 F. Feist, S. L. Walden, J. Alves, S. V. Kunz, A. S. Micallef, A. J. Brock, J. C. McMurtrie, T. Weil, J. P. Blinco and C. Barner-Kowollik, *Angew. Chem., Int. Ed.*, 2021, **60**, 10402–10408.
39 F. Feist, L. L. Rodrigues, S. L. Walden and C. Barner-Kowollik, *J. Org. Chem.*, 2022, **87**, 9296–9300.
40 S. Adhikari, A. Ghosh, M. Ghosh, S. Guria and D. Das, *Sens. Actuators, B*, 2017, **251**, 942–950.

41 C. A. Schneider, W. S. Rasband and K. W. Eliceiri, *Nat. Methods*, 2012, **9**, 671–675.
42 M. T. Gokmen and F. E. Du Prez, *Prog. Polym. Sci.*, 2012, **37**, 365–405.
43 N. Raval, R. Maheshwari, D. Kalyane, S. R. Youngren-Ortiz, M. B. Chougule and R. K. Tekade, in *Basic Fundamentals of Drug Delivery*, ed. R. K. Tekade, Academic Press, 2019, ch. 10, pp. 369–400.